Badar, Tabish; Ouattara, Issouf; Backman, Juha; Visala, Arto

Estimation of 3D form of the Path for Autonomous Driving in Terrain

Published in:
IFAC-PapersOnLine

DOI:
10.1016/j.ifacol.2023.10.1264

Published: 22/11/2023

Document Version
Publisher's PDF, also known as Version of record

Please cite the original version:
Badar, T., Ouattara, I., Backman, J., & Visala, A. (2023). Estimation of 3D form of the Path for Autonomous Driving in Terrain. *IFAC-PapersOnLine*, *56*(2), 4916-4921. https://doi.org/10.1016/j.ifacol.2023.10.1264

Available online at www.sciencedirect.com

ScienceDirect

IFAC PapersOnLine 56-2 (2023) 4916–4921

Estimation of 3D form of the Path for Autonomous Driving in Terrain. ⋆

Tabish Badar * **Issouf Ouattara** * **Juha Backman** *,** **Arto Visala** *

* *Department of Electrical Engineering and Automation, Aalto University, 02150 Espoo, Finland (e-mails: firstname.surname@aalto.fi)*
** *Farming technologies, Natural Resources Institute Finland (Luke), Lönnrotinkatu 7, 50100 Mikkeli, Finland (e-mail: juha.backman@luke.fi)*

Abstract: 3D path estimation, i.e., determining the height profiles of the path, is crucial in motion control for autonomous driving in terrains. It is essential to prevent rollover from abrupt peaks, dips, and briefly wet ground. In this study, wheel displacement measurements and height estimation of an off-road vehicle are presented. A calibration process is suggested to measure the instantaneous vertical displacement of each wheel. GNSS-pose-based methods are used to estimate the vehicle's geometry parameters yielding the centimeter-level accuracy of the 3D-path estimation method. The accuracy of the vehicle's instrumentation is examined on a test track to create a 3D terrain model of the path. The outcome of the proposed scheme is compared to a reference elevation profile created with structure from motion on the basis of machine vision and GNSS using data collected by an unmanned aerial vehicle. The comparison of the results demonstrates that the 3D path can be estimated with sufficient accuracy in open terrain using ground vehicles.

Keywords: 3D terrain model, vehicle instrumentation, ground elevation profile, autonomous ground vehicles, forest machines, structure from motion, UAV mapping.

1. INTRODUCTION

Forests are the most important natural resource in Finland. They cover over 70% of the land with annual growth of around 107 million cubic meters, where only the volume of annually consumed roundwood is 69 million cubic meters (see, for example, Harrinkari et al. (2016) for relevant statistics).

Fig. 1. Polaris e-ATV is shown with LiDAR, SPAN unit, GNSS Antenna, and Omni-directional Camera mounted on top.

A classic machine chain in forest harvesting constitutes a harvester and a forwarder. The harvester is used for felling, debranching, and cutting the stem to length, whereas the forwarder carries the logs to the roadside. Then, the trucks transport the logs to sawmills and factories. However, such a machine chain may seriously damage the forest ground especially when the soil is wet or not completely frozen. Such damage may exacerbate over time due to short winters because of climate change. Thus, lighter forwarders are needed, for example, two autonomous forwarders serving one harvester. In this study, we use Polaris e-ATV, shown in Figure 1, to demonstrate the estimation of the solid form of the ground, which serves as an important precursor for achieving a (semi-)autonomous operation of the classic machine chain.

The literature on ground vehicles is limited to methods that either estimate the road roughness profile (see, for example, González et al. (2008) and the references within) or sudden potholes, such as Xue et al. (2017). In other studies, see, for example, Broggi et al. (2013); Jaspers et al. (2017); Forkel et al. (2021), the basic data used for the estimation of the 3D form of the terrain is a 3D point cloud derived either from LiDAR, a camera, or a combination of these two sensors mounted on the vehicles. However, in winter conditions where the ground is covered with snow, the methods relying on point clouds can only determine the 3D form of the surface of the snow and not the underlying solid ground.

Thus, the idea is that the instrumented harvester, going always first, defines the path and creates the 3D profile for the autonomous forwarder. To attain this goal, rotary position sensors are installed in Polaris e-ATV to measure the vertical displacement of each wheel over the ground. This wheel displacement information is then integrated with the position information from the global navigation satellite system (GNSS) unit and attitude information from the inertial measurement unit (IMU)

⋆ The research is funded by the Technology Industries of Finland Centennial Foundation and Jane and Aatos Erkko Foundation.

10.1016/j.ifacol.2023.10.1264

to estimate the 3D form of the path. Later in real forests, GNSS is not accurate. The accurate positioning is implemented relative to trees with forest SLAM. To validate the results of our study, an unmanned aerial vehicle (UAV) is used to build a reference 3D model of the terrain. The usage of UAVs for creating a 3D terrain model is a mature technology, where the resulting model can achieve centimeter-level accuracy using ground control points, as described in Sanz-Ablanedo et al. (2018); Jiménez-Jiménez et al. (2021). Earlier, the estimated terrain form was only validated using visual results as discussed in Broggi et al. (2013); Jaspers et al. (2017).

The organization of the rest of the document is as follows. Brief details about the problem under study with essential information about Polaris e-ATV are presented in Section 2. The details about the installation of the hardware in the vehicle to obtain wheel height information are provided in Section 3. In the same section, the spring coefficient calibration procedure is highlighted. Section 4 briefly explains the methods to compute the parameters that are crucial to achieving the centimeter-level accuracy of the 3D path estimation. In Section 5, we use the equations to compute the 3D form of the ground as seen by each tire. the results obtained from the novel method are compared to one obtained from camera data using the UAV. Finally, the conclusive remarks are mentioned in Section 6.

2. PROBLEM FORMULATION

Polaris Ranger, as shown in Figure 1, is an e-ATV for research and teaching at Aalto University. It is 143.5 cm wide, 274.3 cm long, and 185.4 cm high above the ground. The front suspensions are MacPherson struts, while the dual A-arm suspension system is installed at the rear axle. Each Carlisle tire has a rating of 25×9–12 with a rated tire pressure of 137.9 kPa. At Aalto University, Polaris e-ATV has been equipped with a state-of-the-art set of sensors, actuators, and electronic control units (ECUs). These ECUs are used for power steering and automatic speed control along with handling data from wheel encoders. In addition, it constitutes a synchronous position, attitude, and navigation (SPAN) unit that combines real-time kinematic (RTK) corrections with GNSS and IMU data. Moreover, Light Detection and Ranging (LiDAR) equipment along with an omnidirectional camera are also installed.

To get the 3D form of the ground, we need to know the position of each wheel in the inertial frame. The equation that describes the position of the wheel-ground contact patch in the inertial frame of reference is given as

$$\mathbf{P}_k = \mathbf{C}_b^G(-\mathbf{P}_{b,\text{OFF}} + \mathbf{P}_{b,k}) + \mathbf{P}_{\text{GNSS}} + \begin{bmatrix} 0 \\ 0 \\ \Delta_k - h_T \end{bmatrix}, \quad (1)$$

where the subscript (k) represents front left (FL), front right (FR), rear left (RL), and rear right (RR) tires or strut-mount points, respectively. In the above equation, $\mathbf{C}_b^G$ is the body frame to a global frame rotation matrix, which is defined as

$$\mathbf{C}_b^G = \mathbf{R}_z(\psi)\mathbf{R}_y(\theta + \theta_{\text{off}})\mathbf{R}_x(\phi + \phi_{\text{off}}), \quad (2)$$

where $\mathbf{R}_x(\cdot)$, $\mathbf{R}_y(\cdot)$, and $\mathbf{R}_z(\cdot)$ are the rotation matrices (see, for example, Etkin and Reid (1995) for their definition). The Euler angles are roll angle (ϕ – positive right-side down), pitch angle (θ – positive front-side down), and yaw angle (ψ – positive counterclockwise). A pitch angle offset θ_{off} and roll angle offset ϕ_{off} is expected due to probable SPAN installation issues on Polaris. Moreover, we define the important position vectors as:

$$\mathbf{P}_{b,\text{off}} = \begin{bmatrix} x_{\text{off}} \\ y_{\text{off}} \\ h_{\text{off}} \end{bmatrix}; \quad \mathbf{P}_{b,k} = \begin{bmatrix} l_k/2 \\ t_k/2 \\ h_k/2 \end{bmatrix}; \quad \mathbf{P}_{\text{GNSS}} = \begin{bmatrix} X_{\text{G}} \\ Y_{\text{G}} \\ Z_{\text{G}} \end{bmatrix},$$

where $\mathbf{P}_{b,\text{off}}$ contains the offset values between the position of the GNSS antenna and the center of the vehicle (CV) in the body frame. $\mathbf{P}_{b,k}$ is the distance of kth tire from CV in body frame. Thus, $l_k/2$ is horizontal, $t_k/2$ is lateral, and $h_k/2 = h_{\text{off}}$ is the vertical distance between the kth center of each wheel and CV. Notice that the position vector $\mathbf{P}_{b,k}$ is defined in terms of wheelbase, track width, and box height after sign adjustments when the origin $(0, 0, 0)$ of the vehicle is assumed to be at the CV. In equation (1), Δ_k represents the instantaneous displacement of the kth spring, and h_T is the tire's diameter.

In this study, we are using positions reported by the SPAN unit, that is, $\mathbf{P}_{\text{GNSS}}$ contains the position information of the GNSS antenna in the global frame. The SPAN unit is capable of incorporating Real-time Kinematic (RTK) corrections from a base station. The RTK corrections are needed to get the positioning data at an accuracy of 1 cm. It is important as the ground truth for the 3D form of the path is provided by an unmanned aerial vehicle (UAV). Other crucial factors influencing the accuracy of the ground form estimation are the parameters $x_{\text{off}}, y_{\text{off}}, h_{\text{off}}, l, t, h_T$, along with θ_{off} and ϕ_{off}. However, the first and foremost step is to compute the displacement Δ_k of the kth spring at each corner of the vehicle.

The instrumentation needed to measure the instantaneous vertical deflection, either compression or relaxation, of each spring is detailed in the next section.

3. POLARIS INSTRUMENTATION

A Hall-effect rotary position sensor was installed on every shaft joining the Polaris' main body to the center of kth wheel such that each sensor translates the vertical displacement of each wheel to voltage in a linearly distributed measurement range. Figure 2a shows the 3D model of the sensor mount created in computer-aided design (CAD) software. Four sensor mount assemblies were printed using a 3D printer and installed on the shaft as shown in Figure 2b. The mounting of the sensors was such that their installation did not require intrusion or welding. Such a design allowed the sensor mounts to be disassembled without leaving permanent changes to the Polaris structures, where the mount assemblies are mirrored from left to right.

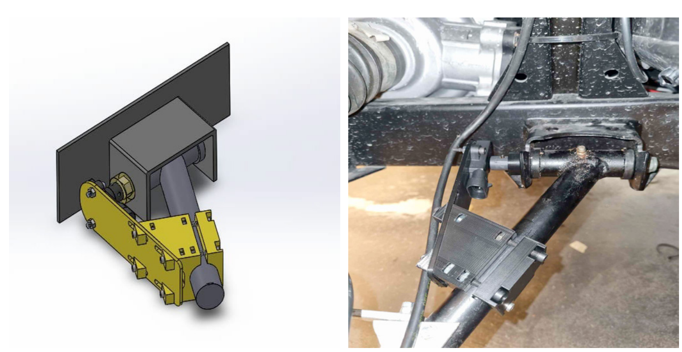

(a) CAD Model. (b) 3D printed sensor mounts.

Fig. 2. **Left**: 3D design of the sensor mount using CAD software is shown. **Right**: The 3D printed assembly is shown mounted on the wheel shaft of Polaris e-ATV.

From Hooke's law, the force exerted on the spring F_s due to its compression or relaxation is given as

$$F_{s,k} = -\mathcal{K}_{s,k}\Delta_k, \quad (3)$$

where $\mathcal{K}_{s,k}$ is the coefficient that describes the stiffness of the kth spring. The strut-mount types in a vehicle are different, especially for front and rear axles, and hence the geometry of the installed springs. As described above, the front suspension system in Polaris is a MacPherson type, whereas the rear suspension system is a dual A-arm type. This directly affects the spring coefficient $\mathcal{K}_{s,k}$, which may be adjusted for each strut based on the vehicle's factory calibration. Therefore, it necessitates designing a test procedure to determine the relationship between spring deflection Δ_k and the sensor voltages in a generalized way without requiring equation (3).

To achieve this, a weighing scale was used to measure the mass of each side of the vehicle while we load or unload that particular side. Through this, the idea is to first acquire a linear relationship between the sensor voltages and the measured height of each wheel side such that

$$H_k = \mathcal{K}_{H,k}V_k + \mathcal{C}_{H,k}, \quad (4)$$

where H_k and V_k are the height above ground and the voltage of the sensor installed at the kth wheel-mount shaft, respectively. For this, a random point near each wheel was selected and the height above ground of the randomly selected reference point was measured using measurement tape. Thus, the coefficients $\mathcal{K}_{H,k}$ and $\mathcal{C}_{H,k}$ describe the linear relationship between H_k and V_k. Furthermore, there is a need to find a relationship between the vertical displacement of each side and the weight of the kth side, such that

$$m_k = \mathcal{K}_{m,k}H_k + \mathcal{C}_{m,k}, \quad (5)$$

where $\mathcal{K}_{m,k}$ and $\mathcal{C}_{m,k}$ are coefficients describing a linear relation between load m_k and height H_k of the randomly selected point near kth wheel.

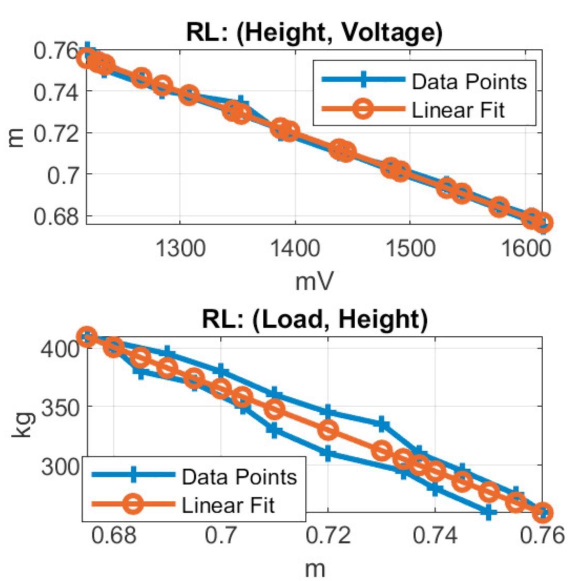

Fig. 3. **Top**: Height on the y-axis versus sensor voltage on the x-axis. **Bottom**: Height on the x-axis versus mass on the y-axis.

Thus, the main objective in this section is to present the calibration routine to determine the coefficients $\mathcal{K}_H$, $\mathcal{C}_H$, $\mathcal{K}_m$ and $\mathcal{C}_m$ for each side of the vehicle. To achieve this, one of the four sides of the vehicle was driven on the weighing scale. Afterward, the kth side was loaded in 10 to 20 kg load increments. Meanwhile, the height above ground for the kth side was noted along with the sensor voltage. Figure 3 shows the calibration results for the rear left (RL) side of Polaris. The blue crosses represent the observed data, whereas the red circles indicate the linear fit when the desired coefficients were found by using the least-squares (LS) method (see Bar-Shalom et al. (2001), where the LS-estimate is found by solving the normal equation). Likewise, the calibration results for the front right (FR) side are depicted in Figure 4.

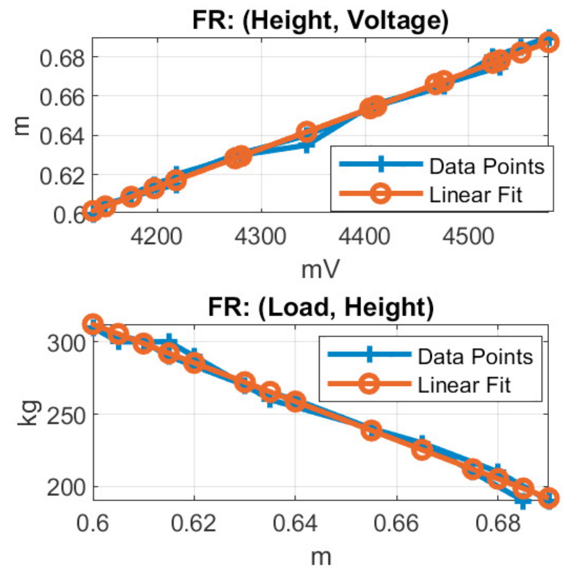

Fig. 4. **Top**: Height on the y-axis versus sensor voltage on the x-axis. **Bottom**: Height on the x-axis versus mass on the y-axis.

Computing the height of each spring when zero mass was applied to each corner gives the initial height $H_{k,0}$ of the kth spring. Since, $m_k = 0$ in equation (5) directly translates to spring force $F_k = 0$ in equation (3), we get

$$H_{k,0} = -\frac{\mathcal{C}_{m,k}}{\mathcal{K}_{m,k}}. \quad (6)$$

In practice, there is no need for height H_k as the measurement point for each H_k is some arbitrary point near kth wheel to calibrate the spring deflections. Thus, we have a linear relationship between the spring deflection and sensor voltages, which is given as

$$\begin{aligned} \Delta_k &= H_k - H_{k,0} \\ &= \mathcal{K}_{H,k}V_k + \mathcal{C}_{H,k} + \frac{\mathcal{C}_{m,k}}{\mathcal{K}_{m,k}}. \end{aligned} \quad (7)$$

Next, we present the methods to find the critical parameters illustrated in equation (1).

4. DETERMINATION OF PARAMETERS

In this section, we present the methods used to determine the vehicle's geometry parameters using RTK-corrected GNSS antenna positions. Firstly, we assume that each tire is inflated at the rated pressure with negligible vertical deflection during the nominal vehicle operations. In other words, we assume a constant $h_T = 0.3175$ m, where its value is obtained from the tire's rating.

Using a measurement tape, the wheelbase (l = 1.834 m) and track width (t = 1.176 m) values were acquired. However, the tape measurement method might not be accurate as we desire a centimeter-level accuracy for our 3D path estimation method that heavily relies on the vehicle's geometry. It is the case that the datasheet of Polaris only provides the wheelbase value, i.e. l =1.83 m, and not the track width. Thus, we ascertain the track width tape measurement by using a GNSS-pose-based method as shown in Figure 5. Initially, Polaris was parked at position $\mathbf{P}_1$ and later moved to position $\mathbf{P}_2$. With this experiment, the idea is to move the right side wheels in $\mathbf{P}_2$ to the same position as the left wheels were in position $\mathbf{P}_1$. Hence, moving the GNSS antenna in the lateral direction by a distance equal to track width. The value of track width obtained from this method is t = 1.160 m. Thus, we choose l = 1.83 m (from the datasheet) and t = 1.160 m (from the GNSS-pose-based method).

(a) $\mathbf{P}_1$ (b) $\mathbf{P}_2$ (c) $\mathbf{P}_3$ (d) $\mathbf{P}_4$

Fig. 5. Initially, Polaris is at position $\mathbf{P}_1$. After a few minutes of data recording, Polaris was driven to position $\mathbf{P}_2$. Then, the vehicle was driven to position $\mathbf{P}_3$. Wheel lifting strategy such as depicted in $\mathbf{P}_4$ was to measure antenna height above CV.

Furthermore, another GNSS-pose-based method was employed where a 180° turn was used to detect the x_{off} and y_{off} from the vehicle's CV. To achieve this, Polaris was parked in $\mathbf{P}_3$ position as highlighted in Figure 5c, i.e., facing opposite to when it was at $\mathbf{P}_1$. This 180° turn provides a mid-point of the vehicle in body coordinates, such that

$$\mathbf{P}_{b,i} = (\mathbf{C}_b^G)^{-1}(\mathbf{P}_i - \mathbf{P}_{\text{MID}}) \tag{8}$$

for $i = \{1, 3\}$, such that

$$\mathbf{P}_{\text{MID}} = (\mathbf{P}_1 + \mathbf{P}_3)/2, \tag{9}$$

and $\mathbf{C}_b^G$ is the body-global frame rotation matrix as defined in equation (2). Thus, the lateral and longitudinal distances between $\mathbf{P}_{\text{MID}}$ and either of $\mathbf{P}_{b,1}$ or $\mathbf{P}_{b,3}$ will provide x_{off} and y_{off} estimates, respectively. By averaging (x, y)-coordinates of $\mathbf{P}_{b,1}$ and $\mathbf{P}_{b,3}$, we get $x_{\text{off}} = -0.4583$ m and $y_{\text{off}} = 0.2587$ m with respect to mid-point.

Next, to get h_{off} estimate, another GNSS-pose-based method involves lifting up each wheel above the ground in a consecutive fashion. Figure 5d depicts the front right (FR) side of the vehicle being lifted above the ground. Thus, the idea is to estimate h_{off} such that the difference between the global position of each wheel at $\mathbf{P}_4$ (when, for example, the FR side is lifted) and at $\mathbf{P}_1$ (initial position) is minimum. Then, a mean square error (MSE) criteria can be defined as

$$\text{MSE} = (\|\mathbf{P}_{1,\text{RL}} - \mathbf{P}_{4,\text{RL}}\| + \|\mathbf{P}_{1,\text{FR}} - \mathbf{P}_{5,\text{FR}}\| + \|\mathbf{P}_{1,\text{FL}} - \mathbf{P}_{6,\text{FL}}\| + \|\mathbf{P}_{1,\text{RR}} - \mathbf{P}_{7,\text{RR}}\|)/4, \tag{10}$$

where $\mathbf{P}_4$ represents the GNSS antenna position when the FR side was lifted up, $\mathbf{P}_5$ when the RL side is lifted up, $\mathbf{P}_6$ for RR side, and $\mathbf{P}_7$ for FL side, respectively. Note that, the minimum of MSE will occur at h_{off}, i.e., when the change in the absolute height of GNSS antenna when the kth wheel was lifted versus when it was at an original position, that is at $\mathbf{P}_1$, is minimum. The important graphs corresponding to the test when the front-right (FR) wheel was lifted is depicted in Figure 6. In this figure, the dotted red curve shows $h_{\text{off,RR}} = \|\mathbf{P}_{1,\text{RR}} - \mathbf{P}_{4,\text{RR}}\|$, blue curve represents $h_{\text{off,RL}} = \|\mathbf{P}_{1,\text{RL}} - \mathbf{P}_{4,\text{RL}}\|$, and the green curve shows $h_{\text{off,FL}} = \|\mathbf{P}_{1,\text{FL}} - \mathbf{P}_{4,\text{FL}}\|$ over the range of h_{off} values. Thus, for the FR-wheel being lifted, the minimum height error value is given as

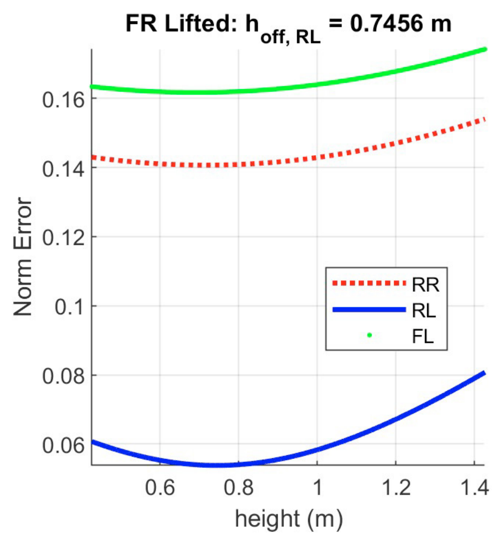

Fig. 6. Results from lifting-up FR wheel shows that the minimum change in height from its initial position at $\mathbf{P}_1$ is found for the (diagonally opposite) RL wheel.

$$h_{\text{min},1} = \min\{h_{\text{off,RR}}, h_{\text{off,RL}}, h_{\text{off,FL}}\} = h_{\text{off,RL}}.$$

Thus, we have the minima $h_{\text{min},1} = h_{\text{off,RL}} = 0.7456$ m for this case. In a similar manner, all other entries in equation (10) were obtained to get an initial estimate of $h_{\text{off}} = 0.8861$ m.

Hitherto, we considered $\theta_{\text{off}} = 0.0°$, $\phi_{\text{off}} = 0.0°$, which might not be the case due to possible SPAN installation issues on Polaris. Thus, we define a parameter vector $\eta = \{x_{\text{off}}, y_{\text{off}}, h_{\text{off}}, \theta_{\text{off}}, \phi_{\text{off}}\}$, and an objective function

$$\mathcal{J} = (4 \times \text{MSE} + E_{1,3} + \sum_k K_k)/9, \tag{11}$$

where MSE is given by equation (10), $E_{1,3} = \|\mathbf{P}_{b,1} - \mathbf{P}_{b,3}\|$ describes the difference between mid-points after 180° turn, and $K_{\text{FR}} = \|\mathbf{P}_{1,\text{FR}} - \mathbf{P}_{3,\text{RL}}\|$, for example, depicts the position error when the front right (FR) side at position $\mathbf{P}_1$ was taken by the rear left (RL) side when Polaris was in $\mathbf{P}_3$, i.e., after 180° turn. Hence, with $\eta_0 = \{x_{\text{off},0} = -0.4583, y_{\text{off},0} = 0.2587, h_{\text{off},0} = 0.8861, \theta_{\text{off},0} = 0.0, \phi_{\text{off},0} = 0.0\}$ being an initial feed to the

MATLAB's **fminsearch** function that minimizes the objective function $\mathcal{J}$, we get an optimal estimate of the parameter vector, i.e., $\eta_{\text{opt}} = \{x_{\text{off,opt}} = -0.4724, y_{\text{off,opt}} = 0.2546, h_{\text{off,opt}} = 0.8767, \theta_{\text{off,opt}} = 0.0002, \phi_{\text{off,opt}} = -0.0001\}$. Note that, by introducing an optimization step, we have validated the values of estimated parameters as well as the methods used to acquire these.

5. 3D-PATH ESTIMATION RESULTS

To detect the elevation profile of the spatial path, Polaris was driven on the test track at Vihti, Finland in clockwise or counter-clockwise directions. A birds-eye view of the test tracks can be observed in Figure 7, which shows two circular test tracks with different elevation profiles made of concrete. In this article, a selected set of data is discussed when the Polaris was driven on the outer track in the counterclockwise direction.

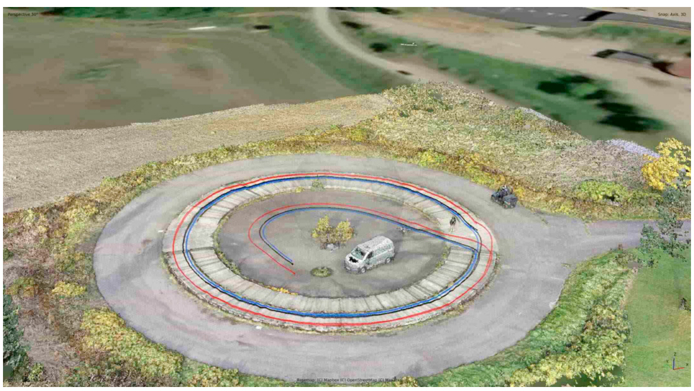

Fig. 7. 3D model of the test track formed in Metashape using RTK-GNSS tagged camera images captured by drone. The GNSS antenna position (shown in black), the FR wheel (in red), and the RL wheel (in blue) paths recorded by Polaris instruments are imported into MetaShape software.

The pose data from SPAN and rotary position sensors were collected for a specific run of Polaris. In Figure 8, $\mathbf{P}_{\text{GNSS}}$ is provided by the SPAN unit, whereas $\mathbf{P}_{\text{FR}}$ and $\mathbf{P}_{\text{RL}}$ are computed by using equation (1). Only position data for FR and RL wheels are shown for the clarity of presentation. It is interesting to note that from the starting points (shown by crosses in Figure 8) onward, the RL wheel position (blue curves) remains closer and to the left of the GNSS position (shown in black). It is due to the reason that the GNSS antenna is installed closer to the left side of the vehicle, which can be observed in Figure 1. Further, notice that the peaks in the elevation profile for the FR side (red graphs in Figure 8) lead in distance traveled as compared to those observed by GNSS and RL wheel.

To produce the reference 3D model, a UAV equipped with a camera is used to capture images. These images are tagged with GNSS position from the onboard positioning unit. The GNSS positions are used as the initial pose of the camera by a structure from motion (SfM) and multi-view stereo matching (MVS) process which further refines the camera poses using the common features detected in different images (see Iglhaut et al. (2019) for a general presentation of the SfM-MVS photogrammetry process). First, a sparse point cloud is built during the camera pose estimation, then a much dense point cloud is built. From

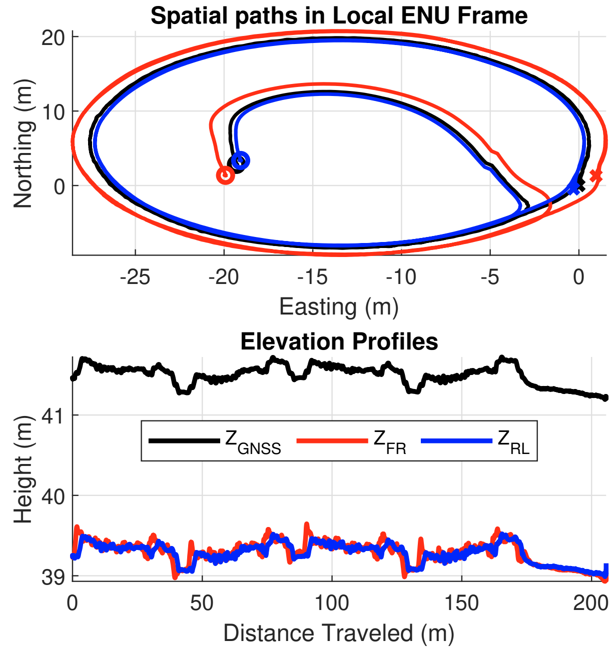

Fig. 8. **Top**: Spatial paths of GNSS antenna (black), FR wheel (red), and RL wheel (blue). The crosses and circles are the starting and finish positions, respectively. **Bottom**: Z_{GNSS} is the altitude output from SPAN, Z_{FR} and Z_{RL} are the elevations computed by equation (1).

the dense point cloud, a depth map is built which can be used to generate a digital elevation model of the terrain.

The MetaShape software, by Agisoft LLC (2019), is used in this study to produce the reference 3D model. To improve the quality of the produced 3D model, 4 ground control points (GCPs) were used. According to Sanz-Ablanedo et al. (2018), using more than 3 GCPs for around 100 images will not improve the accuracy of the obtained 3D model. In this study, the area under consideration is small, thus around 140 images were sufficient to build a 3D model of the test track. The GCPs positions were measured using an RTK GNSS sensor with centimeter accuracy. The position of each ground control point is recorded for at least 30 seconds. The standard deviation of the altitude of the GCPs have values ranging from 2mm to 4mm which indicates a very stable altitude measurement. The produced 3D model from the drone data has color information making it easier to pinpoint some locations on the model and verify their altitude measurement using manual methods. The accuracy of the RTK sensor used and the ability to manually check the altitude results make the 3D model produced from the UAV data a good choice as a reference 3D terrain model. Figure 7 illustrates the resulting 3D model with the overlaid driving trajectories $\mathbf{P}_{\text{GNSS}}$, $\mathbf{P}_{\text{FR}}$, and $\mathbf{P}_{\text{RL}}$ obtained from Polaris e-ATV. The recorded latitude and longitude data of the Polaris e-ATV is projected on the reference 3D model to extract height along the vehicle path. The extracted height data is used as the reference height in this study.

The results obtained from the two methods are highlighted in Figure 9, which illustrates the transients in Z_{FR} and Z_{RL} due to abrupt changes in local altitudes closely following the reference altitudes. The mean and maximum values of the absolute error $|Z_{\text{FR}} - Z_{\text{FR,UAV}}|$ are 2.938 cm and 12.345 cm, respectively.

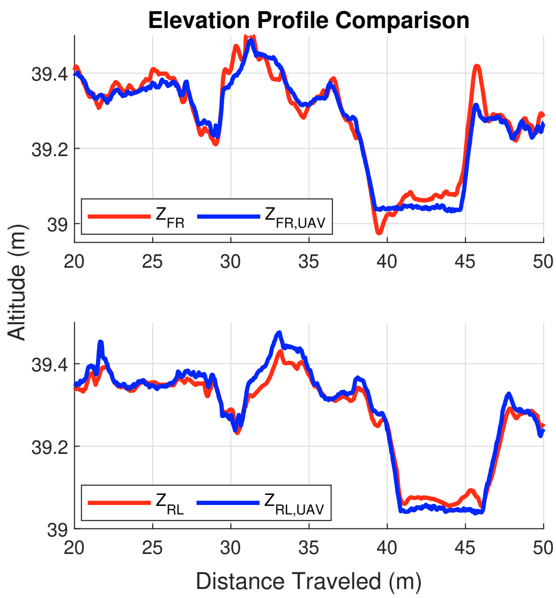

Fig. 9. Results comparing the elevation profiles computed by using Polaris instrumentation (red graphs) with ground truth – UAV data (blue graphs).

While the mean and maximum values for $|Z_{RL} - Z_{RL,UAV}|$ are 1.865 cm and 15.776 cm, respectively. The reasoning for high errors was the high standard deviation of the height measurements reported by SPAN as it lost its centimeter-level positioning accuracy mainly due to problems in the reception of RTK signals.

6. CONCLUSIONS AND FUTURE WORK

The accurate estimation of the 3D form of the solid ground is crucial for the stable operations of off-road vehicles. In this paper, we have presented a tangible method to estimate the 3D form of the ground by using wheel displacement, attitude, and global positioning data. The wheel displacement measurements require an extensive calibration procedure. Likewise, to compute the 3D form of the path as accurately as possible a few vehicle-related parameters are identified. The GNSS-pose-based methods are effective in finding these parameters as a similar method may be applied to bigger forest machines. The data collected from a drive on a test track is analyzed. The ground vehicle's path elevation data is then compared to UAV data. The results are promising and show the effectiveness of the instrumentation in the computation of the 3D form of the path.

In forests, the quality of the positioning data from satellite-based navigation systems is often poor. Moreover, as the GNSS height measurement is generally of low quality, an alternative approach is needed for 3D-path modeling. Thus, when driving forward in a forest, the spatial positioning can be based on trees. In such a scenario, the estimated absolute orientation of the vehicle and the height measurements of the front wheels can be utilized to model the height profile of the path since the rear wheels are simply following the already modeled 3D profile. Therefore, in this paper, the primary approach with wheel height measurements and exact RTK-corrected GNSS pose measurements was implemented and tested. For future work, however, the research question is, do ground vehicles have any means of computing, namely, the elevation profile of the terrain, in GNSS-free environments?

ACKNOWLEDGEMENTS

The authors acknowledge the role of the Department of Electrical Engineering and Automation at Aalto University in making this research possible. Special thanks to the Technology Industries of Finland Centennial Foundation and Jane and Aatos Erkko Foundation for providing necessary funding for the **Autologger** project under The Future Makers program.

REFERENCES

Agisoft LLC (2019). *Agisoft Metashape User Manual, Professional Edition, Version 1.5*.

Bar-Shalom, Y., Li, X.R., and Thiagalingham, K. (2001). *Estimation with Applications to Tracking and Navigation*. John-Wiley and Sons, Inc.

Broggi, A., Cardarelli, E., Cattani, S., and Sabbatelli, M. (2013). Terrain mapping for off-road autonomous ground vehicles using rational b-spline surfaces and stereo vision. In *2013 IEEE Intelligent Vehicles Symposium (IV)*, 648–653.

Etkin, B. and Reid, L.D. (1995). *Dynamics of Flight: Stability and Control*. John Wiley and Sons, USA, third edition.

Forkel, B., Kallwies, J., and Wuensche, H.J. (2021). Probabilistic terrain estimation for autonomous off-road driving. In *2021 IEEE International Conference on Robotics and Automation (ICRA)*, 13864–13870.

González, A., O'brien, E., Li, Y.Y., and Cashell, K. (2008). The use of vehicle acceleration measurements to estimate road roughness. *Vehicle System Dynamics*, 46(6), 483–499.

Harrinkari, T., Katila, P., and Karppinen, H. (2016). Stakeholder coalitions in forest politics: revision of finnish forest act. *Forest Policy and Economics*, 67, 30–37.

Iglhaut, J., Cabo, C., Puliti, S., Piermattei, L., O'Connor, J., and Rosette, J. (2019). Structure from motion photogrammetry in forestry: a review. *Current Forestry Reports*, 5.

Jaspers, H., Himmelsbach, M., and Wuensche, H.J. (2017). Multi-modal local terrain maps from vision and lidar. In *2017 IEEE Intelligent Vehicles Symposium (IV)*, 1119–1125.

Jiménez-Jiménez, S.I., Ojeda-Bustamante, W., Marcial-Pablo, M.d.J., and Enciso, J. (2021). Digital terrain models generated with low-cost uav photogrammetry: Methodology and accuracy. *ISPRS International Journal of Geo-Information*, 10(5).

Sanz-Ablanedo, E., Chandler, J.H., Rodríguez-Pérez, J.R., and Ordóñez, C. (2018). Accuracy of unmanned aerial vehicle (uav) and sfm photogrammetry survey as a function of the number and location of ground control points used. *Remote Sensing*, 10(10).

Xue, G., Zhu, H., Hu, Z., Yu, J., Zhu, Y., and Luo, Y. (2017). Pothole in the dark: Perceiving pothole profiles with participatory urban vehicles. *IEEE Transactions on Mobile Computing*, 16(5), 1408–1419.